Analysis of friction in quantitative micro-elastography

KAI L. METZNER,[1,2,*] Qi Fang,[1,2] ROWAN W. SANDERSON,[1,2] ALIREZA MOWLA,[1,2] AND BRENDAN F. KENNEDY[1,2,3]

[1]*BRITElab, Harry Perkins Institute of Medical Research, QEII Medical Centre, Nedlands, and Centre for Medical Research, The University of Western Australia, Perth, WA 6009, Australia*
[2]*Department of Electrical, Electronic & Computer Engineering, School of Engineering, The University of Western Australia, Perth, WA 6009, Australia*
[3]*Australian Research Council Centre for Personalised Therapeutics Technologies, Perth, WA 6000, Australia*
*kai.metzner@research.uwa.edu.au

Abstract: Quantitative micro-elastography (QME) is a compression-based optical coherence elastography technique capable of measuring the mechanical properties of tissue on the micro-scale. As QME requires contact between the imaging window and the sample, the presence of friction affects the accuracy of the estimated elasticity. In previous implementations, a lubricant was applied at the contact surfaces, which was assumed to result in negligible friction. However, recently, errors in the estimation of elasticity caused by friction have been reported. This effect has yet to be characterized and is, therefore, not well understood. In this work, we present a systematic analysis of friction in QME using silicone phantoms. We demonstrate that friction, and, therefore, the elasticity accuracy, is influenced by several experimental factors, including the viscosity of the lubricant, the mechanical contrast between the compliant layer and the sample, and the time after the application of a compressive strain. Elasticity errors over an order of magnitude were observed in the absence of appropriate lubrication when compared to uniaxial compression testing. Using an optimized lubrication protocol, we demonstrate accurate elasticity estimation (<10% error) for nonlinear elastic samples with Young's moduli ranging from 3 kPa to 130 kPa. Finally, using a structured phantom, we demonstrate that friction can significantly reduce mechanical contrast in QME. We believe that the framework established in this study will facilitate more robust elasticity estimations in QME, as well as being readily adapted to understand the effects of friction in other contact elastography techniques.

1. Introduction

The mechanical properties of tissue play an important role in the onset and progression of many diseases [1–4]. Breast cancer, for instance, is often associated with tumors that are stiffer than surrounding benign tissue [5–7], and arteriosclerosis causes diseased arteries to become thicker and stiffer [8–10]. Therefore, measurement of the mechanical properties of tissue can act as a clinical biomarker in the diagnosis and study of disease [2–4]. Elastography techniques, including atomic force microscopy [11–13], ultrasound elastography [14], magnetic resonance elastography [6,15], and optical coherence elastography (OCE) [16–18], are a set of imaging techniques that enable the objective evaluation of tissue mechanical properties across a range of length scales. This is typically achieved by using an imaging modality to track tissue deformation under an applied load, from which an image of the tissue's mechanical properties, termed an elastogram, can be estimated using an appropriate mechanical model [18]. On the scale of cells, atomic force microscopy provides surface maps of a sample's mechanical properties with nanometer- to micrometer-scale spatial resolution, while on the scale of organs, ultrasound elastography and magnetic resonance elastography provide penetration depths in the centimeter range with spatial

resolution on the scale of millimeters [2]. Optical coherence elastography, OCE, bridges the scale gap between cells and organs, providing a spatial resolution of 5 - 50 μm and a depth penetration of several millimeters [16–18]. OCE has been proposed and demonstrated in various fields, including in ophthalmology [19,20], cardiology [21,22] and oncology [23,24]. OCE techniques are broadly classified based on the loading mechanism used, with shear wave OCE and compression OCE being the most prominent [2]. In shear wave OCE, a local, transient load is applied to the tissue and optical coherence tomography (OCT) is used to measure the phase velocity of the propagating mechanical waves from which elasticity is estimated [2]. In compression OCE, a quasi-static load is applied at the tissue surface and the resulting strain estimated using OCT [16,18]. Compression OCE has been shown to produce high-speed, high-resolution strain images over lateral fields of view (FOV) up to several centimeters [25,26]. However, as the applied stress is not measured, strain imaging provides only a qualitative map of tissue elasticity, making it challenging to compare elasticity between different samples, as well as in the same sample over time [2,18,27]. To address this, quantitative micro-elastography (QME) [28,29] and related techniques [30–32] have been proposed to provide quantitative measurements of tissue elasticity. In QME, elasticity (Young's modulus) is estimated by applying a uniaxial load to the sample, and measuring the resulting 3-D axial strain in the sample, as well as the 2-D axial stress at the sample surface [33–35]. To estimate axial strain, the axial displacement is measured at each pixel in the OCT FOV using phase-sensitive OCT, and linear regression is used to calculate the slope of the axial displacement over a finite depth, typically ∼10 - 100 μm [2,28,29,33,34,36]. To estimate axial stress at the sample surface, a pre-characterized compliant layer with a thickness of ∼500 - 700 μm is placed between an imaging window and the sample prior to compression being applied. For each lateral position, the axial strain in the layer is measured using phase-sensitive OCT and is then related to the stress at the sample surface using the known stress-strain response of the layer material [29,33–35]. QME has been demonstrated in several biomedical applications, including tumor margin assessment in breast-conserving surgery [25,37–41] and mapping cell elasticity in mechanobiology [36,42].

As previously proposed in ultrasound elastography [14], to estimate elasticity in QME, a uniaxial stress distribution is assumed, and shear stress, such as that caused by friction at the contact interfaces, is considered to be negligible [29,33,34]. However, the low penetration depth of QME compared to ultrasound elastography means that any friction at the contact boundaries can reduce deformation of almost incompressible materials such as silicone and soft tissue, and, consequently, affect the accuracy of elasticity in QME elastograms [2,35,43]. To minimize friction, a lubricant, such as silicone oil, is applied at the contact boundaries, reducing shear stresses that act tangentially between the layer, imaging window, and sample [29,33]. However, it is difficult to control the precise quantity of lubricant, and, also, to ensure even distribution across the layer and sample surfaces during acquisition, which can result in inaccurate and spatially-dependent elasticity [27,33,44]. For instance, inadequate lubrication of the imaging window-layer interface results in friction that restricts deformation of the incompressible layer, *i.e.*, axial strain in the silicone layer, resulting in an underestimation of surface stress and underestimation of sample elasticity [33,35,45].

Despite the importance of friction in obtaining accurate estimations of elasticity in QME, a systematic characterization of its effect has not been performed, making it difficult to optimize the imaging protocol and to obtain reliable elastograms. In this paper, we address this by presenting experimental results on silicone phantoms. To achieve this, we first evaluate how lubrication at different interfaces affects elasticity accuracy, demonstrating the importance of lubrication of all contact surfaces. Following this, we assess the ability to accurately estimate elasticity for samples with nonlinear elastic mechanical properties. We then analyze how the viscosity of the lubricant affects the measured elasticity, revealing a trade-off between elasticity accuracy and the temporal stability of the measurements. Based on these analyses, we implement an

optimized QME scanning protocol and demonstrate the capability to accurately estimate a range of elasticities (Young's modulus of ~3 - 130 kPa). Furthermore, we perform QME on a silicone phantom comprising a stiff inclusion embedded in a softer bulk material, demonstrating how friction can reduce mechanical contrast, and, also, the capability to generate accurate elastograms of mechanically heterogeneous samples using the optimized QME scanning protocol.

2.   Friction in QME: problem definition

In elastography, several assumptions are typically made to simplify the mechanical model, allowing for direct estimation of mechanical properties from the measured displacement or velocity [2]. For instance, in QME, as is the case for most compression elastography techniques, it is assumed that the sample is incompressible and exhibits homogeneous, isotropic, linear elastic behavior. Furthermore, under the assumption of uniaxial stress, QME estimates spatially-resolved Young's modulus, E, at each point in the imaging FOV from the ratio of the axial stress (σ_z), estimated from the deformation of the compliant layer, to the measured axial strain within the sample (ε_z) [29]:

$$E = \frac{\sigma_z}{\varepsilon_z} \tag{1}$$

Importantly, by assuming uniaxial stress, any shear stresses that act perpendicular to the axis of loading, are considered to be negligible. However, shear stresses can be introduced due to the presence of friction, which is a force that acts to oppose the relative motion of two surfaces, arising from factors such as adhesion, capillary forces, and topological contact of asperities between surfaces [46,47]. Given that most tissues, and compliant layers used in QME are incompressible, *i.e.*, they have a Poisson's ratio close to 0.5, lateral expansion, *i.e.*, normal lateral strain, results from axial deformation [5,35,48,49]. Generally, in QME, a lubricant is applied at the contact surfaces, and it is assumed that friction is negligible, *i.e.*, the lateral, and, therefore, axial deformation of the layer and sample is not opposed. However, the presence of friction at the contact surfaces restricts the lateral deformation of the layer and sample, which, together with incompressibility, results in shear stresses, requiring a larger load to be applied to achieve a given strain than is accounted for in the mechanical model. In addition, spatial variations in friction caused, for example, by variations in lubrication, can introduce non-uniform stress and strain, regardless of the mechanical properties of the sample [48]. Consequently, in the presence of friction, the assumption of uniaxial stress, and, thus, the mechanical model used to estimate elasticity is challenged, and can result in errors in the estimation of elasticity in QME.

The impact of friction on measured elasticity is illustrated in Fig. 1, where the deformation of a homogeneous layer and sample with matched elasticity is shown without and with friction between the window-layer, layer-sample, and sample-stage boundaries. Figures 1(a) and 1(b) illustrate the typical deformation of the layer and sample after the application of a compressive load without and with friction, respectively. Figure 1(c) depicts a representative illustration, based on previous experiments and simulations [48], of the axial displacement versus depth in the layer and sample, applied using a piezoelectric actuator, along the central region of both, at the locations indicated by the green (frictionless) and orange (frictional) dashed lines in Figs. 1(a) and 1(b), respectively, where the axial stress is the same in both cases [48]. In Fig. 1(c), the strain (ε), calculated as the gradient of displacement with depth, in both the layer and sample for the frictionless and frictional conditions is highlighted by solid black lines. Figures 1(d) and 1(e) show representative elastograms for both frictionless and frictional contact, respectively.

In the case of frictionless contact, the absence of a force opposing the relative lateral motion of the incompressible layer and sample, allows for unobstructed lateral expansion during compression (Fig. 1(a)). It has been previously demonstrated that this results in a uniform stress distribution in the central region of the layer and sample, and that the axial displacement of the layer and sample, (shown by the green line in Fig. 1(c)) are dependent only on their elasticity [48]. In this
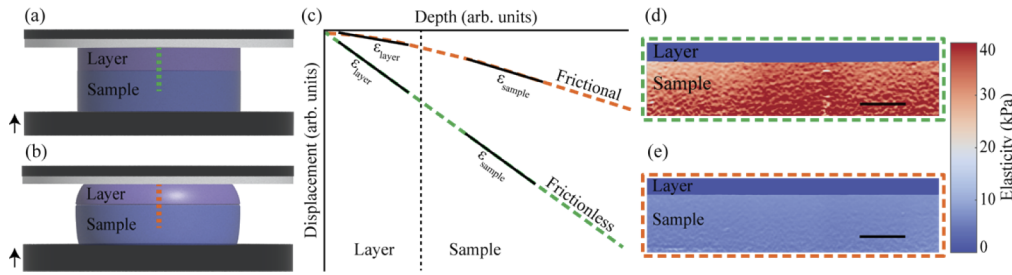
Fig. 1. The effect of friction in QME. (a) and (b) show the deformation of the layer and sample under a uniaxial compressive load, indicated by the vertical black arrows, with (a) frictionless and (b) frictional contact. (c) Plot of the layer and sample axial displacement with depth for frictionless (green line) and frictional (orange line) contact. Additionally, the strain (ε) in the layer and sample for frictionless and frictional contact is indicated as the slope of solid black lines. The vertical dashed line in (c) illustrates the boundary between the layer and the sample. (d) and (e) show representative experimental B-scan elastograms of a homogeneous sample corresponding to (d) frictionless and (e) frictional contact. Scale bars represent 500 μm.

case, the strain measured in the layer and sample is equal, reflecting their matched mechanical properties. This scenario results in accurate elasticity estimation in QME (Fig. 1(d)), where the measured sample elasticity (36.8 kPa ± 5.2 kPa) corresponds well with the elasticity measured using bulk compression testing (38.3 kPa).

For frictional contact, the lateral expansion of the incompressible layer and sample is constrained by opposing frictional forces at the contact boundaries. This effect is illustrated in Fig. 1(b), which shows barrelling of the layer and sample, characteristic of the restriction of lateral expansion due to friction between the layer, sample, imaging window and translation stage [50–52]. Consequently, for the incompressible layer and sample, the restriction of lateral expansion introduces shear stresses that, for a given load, results in lower axial strain in the layer and sample (Fig. 1(c)). This is particularly apparent for friction acting between the deformable layer and rigid imaging window, which significantly limits the lateral expansion of the layer, and, thus, the axial strain, as detailed further in Section 4.1. The reduction in strain in the layer leads to an underestimation of the applied stress, and, in turn, an underestimation of elasticity, shown in Fig. 1(e), of 6.2 kPa ± 0.6 kPa compared to 38.3 kPa measured with bulk compression testing. In addition, for frictional contact, the strain in a layer and sample with equal elasticity is no longer uniform, resulting in a variation in mechanical behavior in and between the layer and sample. Non-uniformity of strain in a homogeneous sample, occurring both laterally as a result of variations in lubrication, and axially with increasing distance from the frictional boundary, leads to the estimated elasticity being spatially dependent.

3. Materials and methods

3.1. QME system and procedure

A schematic diagram of the QME experimental setup is shown in Fig. 2(a). Imaging was performed using a fiber-based spectral-domain OCT system (TEL320, Thorlabs Inc., USA) containing a superluminescent diode light source with a central wavelength of 1300 nm and a spectral bandwidth of 170 nm, providing an imaging depth of 3.5 mm (in air) and a measured axial resolution of 4.8 μm (full width at half maximum (FWHM) in air). The objective scan lens (LSM03, Thorlabs Inc., USA) has a maximum FOV of 9.4×9.4 mm^2 and a measured lateral resolution of 7.2 μm (FWHM). OCT scanning was performed in a common-path configuration, providing a measured displacement sensitivity of 1.4 nm at an OCT signal-to-noise ratio (SNR)

of 40 dB [26]. The reference reflection was provided by partial reflections of the beam from the bottom interface of a 75 mm diameter imaging window (62606, Edmund Optics Inc., USA). The compliant layer and sample were placed between the imaging window and a rigid plate, which was attached to a motorized translation stage (MLJ150, Thorlabs Inc., USA). The translation stage was used to apply a pre-strain to the layer and sample to ensure even contact prior to QME acquisition. Micro-scale compressive loading was then achieved by attaching the imaging window to a piezoelectric ring actuator with an aperture of 65 mm (Piezomechanik GmbH, Germany). The actuator was driven by a waveform generator (33500B Trueform Waveform Generator, Keysight Technologies, USA) connected to a high voltage amplifier (LE200/070, Piezomechanik GmbH, Germany). The actuator was driven with a square wave in the quasi-static regime, *i.e.*, a frequency ≤ 10 Hz [53], synchronized with OCT imaging, such that consecutive B-scans were acquired at different states of mechanical loading. Lubrication of the contact interfaces (*i.e.*, window-layer, layer-sample, and sample-stage) was achieved using ~50 μL of polydimethylsiloxane (PDMS) silicone fluid (Wacker Chemie AG, Germany) with calculated kinematic viscosities of 10, 50, 100, 316, and 1000 $\mathrm{mm^2 s^{-1}}$ (Fig. 2(b)), respectively, henceforth referred to as Lubricant 1 to Lubricant 5. The preparation of the lubricants is described in Section 3.3.
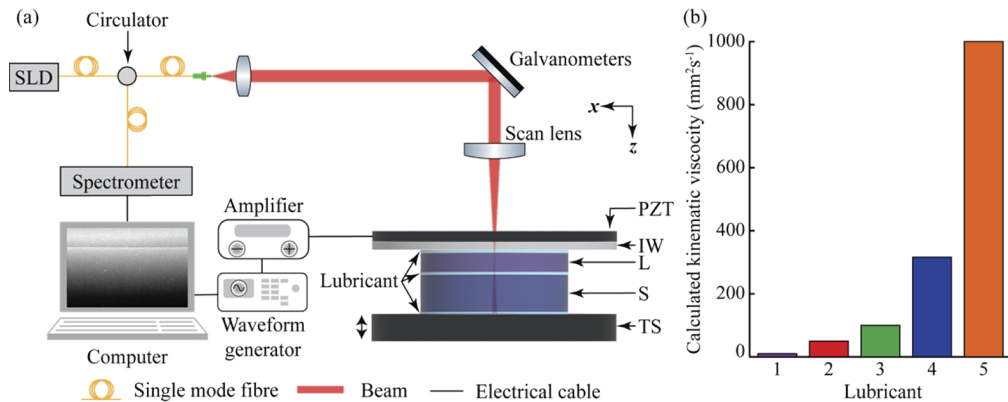

Fig. 2. (a) Experimental setup of the QME system, including: SLD: superluminescent diode, IW: imaging window, PZT: lead zirconate titanate ring actuator, L: layer, S: sample, TS: translation stage. (b) Calculated kinematic viscosities of PDMS silicone fluids used for lubrication.

In this study, B-scans were acquired at a frequency of 20 Hz, each comprising 1,000 A-scans acquired at a frequency of 25 kHz over a 4 mm FOV. At each *y*-location on the sample, after the application of a pre-strain, a pair of B-scans were acquired in the loaded and unloaded state of micro-scale compression. For the experiments described in Sections 4.1, 4.2, 4.4 and 4.5, pairs of B-scans were acquired from 50 locations over 100 μm in the *y*-direction, corresponding to an acquisition time of ~5 seconds. In Section 4.3, to analyze the temporal effect of lubricant viscosity, B-scan pairs were acquired at a single *y*-location for several minutes. For each B-scan pair, the vector difference of the OCT complex data at each pixel location was calculated. For the results presented in Sections 4.1, 4.2, 4.4 and 4.5, the vector difference was spatially averaged over the 50 locations in the *y*-direction. For the results presented in Section 4.3, the vector difference from five B-scan pairs was temporally averaged, resulting in a single measurement of vector difference per second. To further reduce noise, a 2-D Gaussian filter with a FWHM kernel size of 20 μm (lateral) $\times$ 10 μm (axial) was convolved with the vector difference. The resulting phase angle was calculated from the filtered vector difference, and the axial displacement estimated, as described previously [54]. The local strain was calculated in both the layer and the sample using

1-D weighted least squares (WLS) linear regression of displacement with respect to depth over a fitting length of 29 pixels, corresponding to ∼70 μm in both silicone and tissue, assuming a refractive index of ∼1.4 [33,54,55]. In addition to the local strain, the bulk strain of the compliant layer was calculated from the OCT intensity at each lateral position in the B-scan by comparing initial thickness and pre-strained thickness using Canny edge detection [29,56]. From the bulk layer strain, and additionally, the axially averaged local strain in the middle 250 μm of the layer at each lateral position, the applied local stress in the layer was calculated from the pre-characterized stress-strain response of the layer [29]. The tangent modulus, or equivalently, Young's modulus under the assumption of linear elasticity, was determined by dividing the local stress in the layer by the local strain in the sample [35,57,58]. To remove high spatial frequency noise in the elastogram, a median filter of 20 μm (lateral) × 12.5 μm (axial) was applied.

3.2. Silicone phantom and compliant layer fabrication

To investigate friction in QME, compliant silicone layers with Young's modulus of 14.2 kPa and homogeneous phantoms with six different Young's moduli (from 3 kPa to 130 kPa) were fabricated from vulcanizing silicone elastomers (Elastosil P 7676 and Silpuran 2400, Wacker Chemie AG, Germany). The elasticity of the compliant layer and phantoms was controlled by varying the elastomer type, mixing ratio, and by adding a non-crosslinking PDMS oil to the elastomer mixture [55]. The mechanical properties of the layers and phantoms were characterized using a custom uniaxial compression device comprising a load cell (LSB200, FUTEK, USA) and motorized translation stage (MTS25-Z8, Thorlabs Inc., USA). The Young's modulus of the layer, as measured in the linear elastic region, was 14.2 kPa, while Young's moduli of the phantoms ranged from 3 kPa to 130 kPa, which is representative of the elasticity of many biological tissues [1,5,7]. In general, to maximize the elasticity dynamic range, the mechanical properties of the layer should be chosen to closely match that of the sample [29]. In this study, in accordance with previous work, the Young's modulus of the layer has been chosen to match the mechanical properties commonly found in soft tissues, such as adipose tissue [5,7,29,34,37,39]. All phantoms were fabricated as cylinders with a diameter of 6 mm and a thickness of 3 mm, while the compliant layer was fabricated to have a diameter of 6 mm and a thickness of 500 μm. To investigate the effects of friction on mechanically heterogeneous samples, an inclusion phantom was fabricated, containing a stiff cubic inclusion with Young's modulus of 66.5 kPa and side lengths of ∼1 mm, embedded 500 μm below the surface of a softer bulk with Young's modulus of 38.3 kPa.

To provide optical backscattering from the layer and phantoms, titanium dioxide particles (Product No. 232033, Sigma Aldrich, USA) were added to the layer, homogeneous samples, and inclusion, prior to curing, and mixed at concentrations of 0.25 mg/ml, 1 mg/ml and 5 mg/ml, respectively. In contrast to previous studies, which did not utilize layers with added scatterers [25,29,33,42], in this study, scatterers were added to the layer to provide improved visualization of deformation in the layer, which was important to analyze the effect of friction in the layer [35].

For consistency, in the results presented in Sections 4.1 - 4.3, the same layer and sample combination was used, with Young's moduli of 14.2 kPa and 38.3 kPa, respectively, while in the results presented in Section 4.4 to validate the accuracy of QME, the same layer was used, but the samples had different elasticities (Young's moduli of 3 kPa to 130 kPa).

3.3. Lubrication

In QME, as described above, friction is reduced by maintaining a film of lubricant between adjacent surfaces, in particular the window-layer, layer-sample, and sample-stage interfaces, reducing direct contact, and, thus, the transfer of shear forces across the contact boundary. The viscosity is an important characteristic of a lubricant, defined as the ratio of the shear stress and velocity gradient within the lubricant. In other words, the viscosity of a lubricant represents the force transmitted across the lubricant as a result of relative motion. As such, lubricants with low

viscosity are more effective in reducing friction at contact boundaries, as they minimize shear stresses that restrict the lateral deformation of incompressible samples. However, lubricants with low viscosity are more easily exuded from the contact boundaries when a force is applied to the sample, removing the thin film between the surfaces that is required to reduce friction [33,58]. In addition, the time-dependent exudation of the lubricant, which is also dependent on viscosity, causes temporal variations in friction, and, therefore, estimated elasticity [33]. On the other hand, lubricants with high viscosity are more effective in maintaining a stable film of lubricant between the contact boundaries when a mechanical load is applied, however, this results in larger frictional shear forces. As such, it is not straightforward to minimize friction in QME experiments.

To investigate the impact of lubricant viscosity on friction in QME experiments (Section 4.3), five lubricants were created by blending a binary mixture of PDMS silicone fluids with known kinematic viscosities of 10 mm^2s^{-1} and 10,000 mm^2s^{-1} (AK 10 and AKF 10,000, Wacker Chemie AG, Germany). The viscosity of these lubricants was estimated using the Arrhenius equation [59]:

$$\ln(\eta) = x_1 \ln(\eta_1) + x_2 \ln(\eta_2) \tag{2}$$

where $x_{1,2}$ and $\eta_{1,2}$ represent the molar fraction and viscosity of the two base lubricants, respectively. Using this equation, lubricants with viscosities of 10, 50, 100, 316, and 1000 mm^2s^{-1} were created, as presented in Fig. 2(b).

3.4. Image quality metrics in QME

To compare elastogram quality for different friction conditions, we define elasticity accuracy and elasticity sensitivity. Elasticity accuracy is defined by:

$$Accuracy = 1 - \frac{|\bar{E}_{QME} - E_{exp}|}{E_{exp}}, \tag{3}$$

where $\bar{E}_{QME}$ is the mean QME elasticity, calculated by averaging the estimated elasticity in a region of interest, and E_{exp} is the expected elasticity, determined from uniaxial compression testing.

The elasticity sensitivity, previously defined as feature sensitivity [33] is defined as:

$$Sensitivity = \sqrt{\frac{1}{N-1} \sum_{i=1}^{N} |E_i - \bar{E}|}, \tag{4}$$

for a homogeneous region of interest in the sample containing N measurements of elasticity, E, with a mean elasticity $\bar{E}$.

In the calculation of elasticity accuracy and elasticity sensitivity, a region of interest of 1 mm (lateral) × 0.5 mm (axial) in the elastogram was used for Sections 4.2 - 4.4, whilst in Section 4.1, an axial range of 0.9 mm was used to reflect the depths shown in Figs. 3(a) - 3(d). A smaller region of interest of 0.5 mm × 0.25 mm was used in Section 4.5 to allow for the calculation of elasticity in the inclusion and bulk of the heterogeneous sample.

4. Results

4.1. Analysis of lubrication conditions in QME

To examine the impact of friction and to establish the need for lubrication in QME, we analyzed the deformation in the layer and sample, and, also, the accuracy of QME under various lubrication conditions. Four QME scans were performed in which the application of a lubricant with a kinematic viscosity of 50 mm^2s^{-1} (Lubricant 2) [33,42,44,48,58] was varied at the window-layer and layer-sample interfaces. QME was initially performed with no lubrication at either interface,

followed by experiments with lubrication applied at the layer-sample interface only, at the window-layer interface only, and at both interfaces, as shown in Figs. 3(a) - 3(d), which present the strain maps for each scenario. It should be noted that in each scenario, lubricant was applied between the sample and translation stage (*i.e.*, the base plate), as this interface is well beyond the OCT imaging depth and was considered to have negligible impact on surface friction in QME. In each scenario, a pre-strain was applied until uniform contact was made between the imaging window, layer and sample. The estimated local strain was averaged over the central 1 mm in the lateral direction (indicated by the dashed vertical lines in Figs. 3(a) - 3(d)) and plotted with respect to depth (Fig. 3(e)). Furthermore, the estimated elasticity with depth is shown in Fig. 3(f), allowing for comparison to the expected elasticity measured from uniaxial compression testing (indicated by the horizontal dashed line in Fig. 3(f)). Figures 3(a) - 3(f) present data to a sample depth of ~0.9 mm which ensures that strain and elasticity are analyzed in regions of relatively high OCT SNR, *i.e.*, > 10 dB.
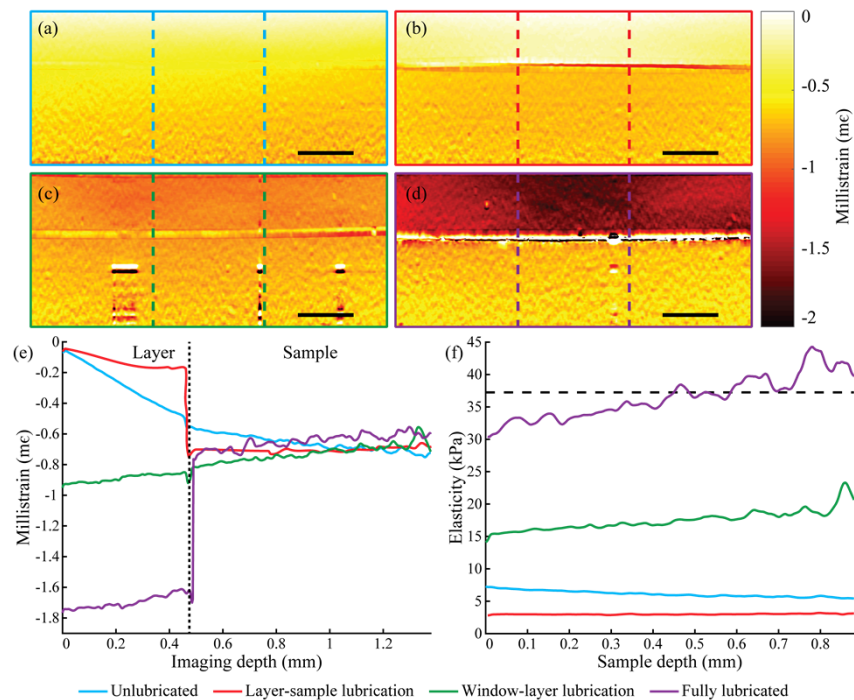

Fig. 3. The impact of lubrication on QME. (a) - (d) Strain maps for different lubrication conditions, namely: (a) unlubricated contact surfaces; (b) lubricant only between the layer and sample; (c) lubricant only between the imaging window and layer; (d) lubricant between the imaging window and layer and between the layer and sample. (e) Plot of the axial strain with imaging depth averaged between the dashed lines in (a) - (d) for the different lubrication conditions. The dashed line in (e) illustrates the boundary between the layer and the sample. (f) Elasticity with depth in the sample for different lubrication conditions. Note that the plots in (e) and (f) have been color-coded, corresponding to the different lubrication conditions, as shown in (a) - (d). The dashed line in (f) represents the expected sample elasticity measured with uniaxial compression testing. Scale bars represent 500 μm.

Without lubrication (Fig. 3(a)), the mean elasticity and elasticity sensitivity over the depth shown in Fig. 3(f) was estimated to be 6.1 kPa and 0.5 kPa, respectively, an underestimation by a factor of 6.3 compared to the expected elasticity of 38.3 kPa. In the unlubricated case, the strain in the layer is heavily influenced by friction. At the interface with the rigid imaging window,

high friction between the window and layer restricts the lateral expansion of the layer. As a result, the layer shows negligible axial strain adjacent to this boundary (blue line in Fig. 3(e)) and increases with depth as the impact of friction decreases. Similarly, friction at the layer-sample interface results in mechanical coupling between the two materials, *i.e.*, where the deformation of one material is dependent on the adjacent material. This is illustrated by depth-dependent strain across the layer-sample boundary, where shear stress, a result of friction acting between the incompressible layer and sample, prevents the layer and sample from deforming independently. In the estimation of elasticity in Eqn. 1, based on the reduced strain in the layer resulting from friction between the layer and the imaging window, the axial stress (σ_z) is underestimated, and consequently, the elasticity of the sample is underestimated. In addition, friction between the layer and sample causes the strain, and, thus, elasticity of the sample to be depth-dependent. This is observed as a decrease in elasticity with depth from 7.3 kPa at the layer-sample surface, to 5.8 kPa at a depth of 0.8 mm below the surface of the sample, as seen from the slope in the blue line in Fig. 3(f).

In Fig. 3(b), lubrication was applied at the layer-sample interface. This resulted in an underestimation of sample elasticity by a factor of 12.7, with a mean elasticity and elasticity sensitivity of 3.0 kPa and 0.1 kPa. Given that lubricant is applied between the layer and sample, friction, and, thus, shear forces acting between the layer-sample boundary are reduced, allowing the two materials to deform independently of one another. This is indicated by a step change in axial strain across the layer-sample boundary (red line in Fig. 3(e)). As a result, the lateral expansion of the sample is independent of the layer deformation, leading to relatively uniform sample strain with depth (standard deviation <0.02 mε). However, given that lubricant is not applied at the window-layer interface, as in the unlubricated case described above, the lateral expansion, and, thus, strain in the layer is restricted by friction acting between the layer and rigid imaging window. Consequently, the stress from the layer is underestimated, while the sample strain is comparatively increased, resulting in a decreased sample elasticity consistent with Eqn. 1.

When lubricant is applied only at the window-layer interface (Fig. 3(c)), the mean sample elasticity and elasticity sensitivity was estimated to be 17.5 kPa and 1.5 kPa respectively, an underestimation by a factor of 2.2. It can be observed that, unlike the previous two results, the influence of friction from the imaging window in reducing strain in the layer and sample is significantly reduced. As such, the stress estimated from the layer is increased, increasing the estimated elasticity of the sample, consistent with Eqn. 1. However, despite the reduction in error compared to the previous two results, under these lubrication conditions, the resultant elasticity is heavily influenced by the difference in Young's modulus of the layer and the sample. This is because friction acting between the layer and sample results in mechanical coupling of the deformation, and, thus, strain across their boundary (green line in Fig. 3(e)). Therefore, the strain distribution shows a gradient in depth from −0.85 mε at the surface of the sample to −0.68 mε at a depth of 0.8 mm. Given that the estimated elasticity in QME is dependent on the mechanical response of the sample in reference to the compliant layer, mechanical coupling between the layer and sample incorrectly suggests that they possess comparable elasticity, likely resulting in an estimated sample elasticity that closely resembles the layer elasticity (14.2 kPa). As a result, the use of either a softer or stiffer layer would likely arbitrarily decrease or increase the estimated elasticity of the sample, respectively.

Lastly, when lubricant was applied at both the window-layer and layer-sample interfaces (Fig. 3(d)), the mean sample elasticity and elasticity sensitivity was estimated to be 36.5 kPa and 3.3 kPa, respectively, an underestimation by a factor of 1.05, corresponding to an error of 5%. In this case, friction, and, thus, shear stresses acting across the window-layer and layer-sample interfaces, are minimized. Consequently, the lateral deformation and resulting strain of the layer and sample are largely independent. This is indicated by the step change in strain across the

layer-sample boundary (purple line in Fig. 3(e)), with a strain contrast that reflects the difference in their elasticity. Note that the strain in the layer and sample both exhibit depth dependence. This is likely attributed to residual mechanical coupling between the layer and sample, indicating that friction, and, therefore, the presence of spatially-dependent shear stresses, might not be fully eliminated. Moreover, translation-induced phase decorrelation increases with depth, as the relative displacement between the reference and sample increases, as well as for increased layer and sample strain [49]. As a result, decorrelation for higher layer strain in the fully lubricated case leads to increasing variation in the measured phase, and consequently displacement, biasing the estimation of strain toward zero and resulting in a decrease of strain with depth.

These results indicate that in the absence of appropriate lubrication of the contact surfaces, the estimated elasticity using QME is not in agreement with the expected sample elasticity. With lubrication of all surfaces, the effects of surface friction are significantly reduced to ensure accurate QME measurements, however, it should be noted that the elasticity sensitivity is also reduced, in agreement with a previous study by Li *et al.* [33]. The reduction in sensitivity with lubrication has been attributed to two phenomena, namely, the temporal variation in elasticity caused by lubricant exudation [33], explored further in Section 4.3, as well as increased phase decorrelation noise, resulting from higher layer and sample strains for fully lubricated scans [49].

4.2. Analysis of pre-strain in QME

In the previous section, to allow for the visualization of a lubricant film, pre-strain was applied until uniform contact was made between the imaging window, layer and sample. However, in compression OCE, pre-strains of up to 20% have been applied to the layer and sample [23,26,29,36,45], and separately, acquisition over a continuous range of strains has been performed to account for the nonlinear elastic properties of samples [39,60]. In this section, we analyze the accuracy of QME in observing the nonlinear elastic behavior of a silicone phantom by estimating the elasticity at increasing sample strain. At each pre-strain, knowing the applied displacement to the layer and sample, and by measuring the layer displacement from OCT (described in Section 3.1), the strain in the layer and sample were calculated based on the change in thickness from the initial, known thickness. Additionally, the applied stress at each pre-strain was estimated using the layer strain and the pre-characterized mechanical properties of the layer.

As demonstrated in Section 4.1, to reduce friction between the imaging window, layer and sample, Lubricant 2 was applied at all contact surfaces. Acquisition was performed at increasing pre-strains using single, or once-off, lubrication, where lubricant was applied before the initial strain, however, not between subsequent strains, as well as repeated lubrication, where lubricant was re-applied at each strain. The elasticity was estimated from a 1 mm (lateral) × 0.5 mm (axial) region, 100 µm below the sample surface. Figure 4 presents the results of estimated elasticity for single lubrication (orange) and repeat lubrication (blue) for increasing sample strain, along with the expected elasticity (solid black line), measured using uniaxial compression testing.

For the case of repeated lubrication, the estimated elasticity is within 6% of the expected elasticity, with a mean error of 3.2%, accurately measuring the nonlinear elastic mechanical response of the silicone phantom over the range of measured strain. In contrast, acquisition using single lubrication is accurate to <3% error at the initial sample strain, however, thereafter, exhibits a decrease in estimated elasticity, and, therefore, reduced accuracy. The decrease in the estimated elasticity up to ~5% sample strain is likely attributed to the temporal exudation of lubricant, with ~20 seconds elapsing between each subsequent acquisition. As a result, the film of lubricant required to reduce friction between the imaging window, layer and sample is removed, leading to an increase in friction, and, therefore, an underestimation of elasticity consistent with the results presented in Section 4.1. At sample strain above ~5%, the estimated elasticity reaches a steady state, potentially signifying that the lubricant has been fully expelled from the contact surfaces. As such, friction does not allow for the estimated elasticity to reflect
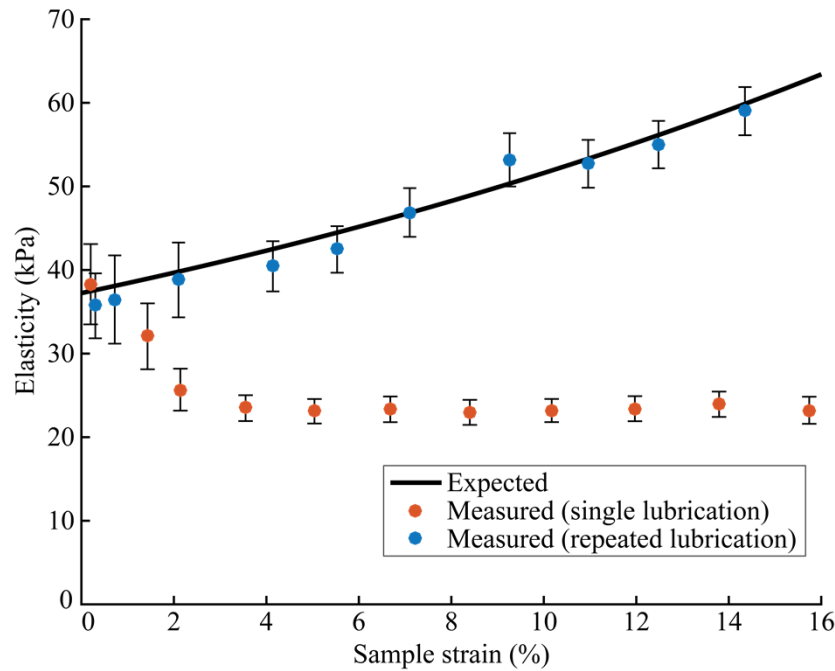
Fig. 4. Estimation of the elasticity of a nonlinear elastic homogeneous silicone phantom for single lubrication (orange) and repeated lubrication (blue). The solid black line represents the expected sample elasticity measured with uniaxial compression testing.

the nonlinear elastic mechanical response of the sample. Importantly, the increasing error in the estimated elasticity from <3% at the initial sample strain, to an underestimation of more than 2.5 times at a sample strain of ∼16% demonstrates that friction, and, therefore, the accuracy of QME, has significant temporal dependence. The extent of this effect likely depends on the viscosity of the lubricant, with higher viscosity lubricants better able to maintain a film of lubricant at the expense of increased friction, as well as the time since the pre-strain was applied, introducing temporal exudation of lubricant. These two aspects are further investigated in Section 4.3.

4.3. *Analysis of lubricant viscosity in QME*

From previous QME studies, it is not clear how the viscosity and temporal exudation of the lubricants used impact friction, and, therefore, the accuracy of QME. In this section, we address this by performing QME measurements on a homogeneous phantom using the five lubricants described in Section 3.3. In each case, a pre-strain was applied until uniform contact was made between the imaging window, layer and sample, separated by a thin film of lubricant. To allow for the comparison between different lubricants, a QME scan was acquired for six minutes, and the mean elasticity estimated from a 1 mm (lateral) × 0.5 mm (axial) region, 100 µm below the sample surface (Fig. 5(a)).

In all cases, other than the most viscous lubricant (Lubricant 5), the elasticity measured using QME shows significant temporal dependence. This is a consequence of the exudation of the lubricant film between the contact surfaces over time, diminishing the effectiveness of the lubricant and resulting in increased friction. As a result, a decrease in the measured elasticity is observed consistent with the frictional behavior described in Section 4.1. As expected, the rate at which the measured elasticity changes correlates with the viscosity of the lubricant, with lower viscosity lubricants showing a more rapid change in the measured elasticity. This can be
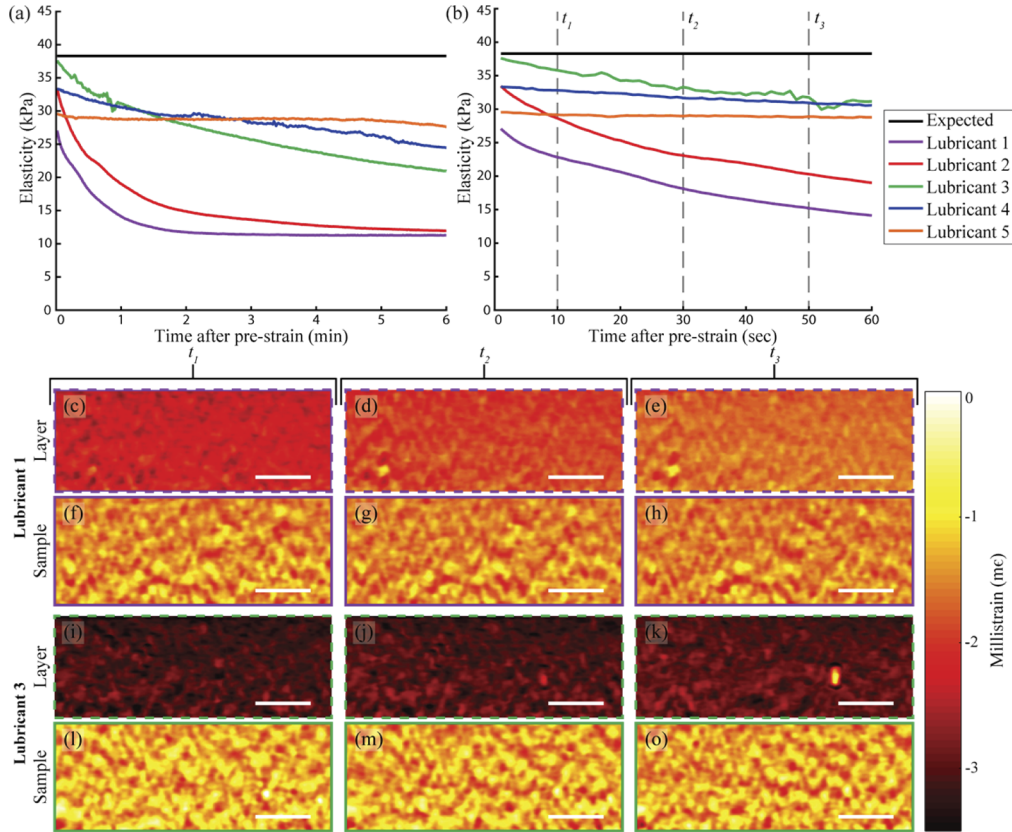
Fig. 5. The impact of lubricant viscosity on QME. (a) and (b) show plots of the mean sample elasticity over time for lubricants with different viscosities over (a) six minutes and (b) one minute. Note that the horizontal black line represents the expected sample elasticity measured with uniaxial compression testing. (c) - (e) The layer strain and (f) - (h) sample strain measured at three different times using Lubricant 1, where (c) and (f) show the strain after $t_1 = 10$ seconds, (d) and (g) after $t_2 = 30$ seconds, and (e) and (h) after $t_3 = 50$ seconds, corresponding to the times shown by the vertical lines in (b). Similarly, (i) - (k) show the layer strain and (l) - (o) the sample strain for Lubricant 3, where (i) and (l) show the strain after $t_1 = 10$ seconds, (j) and (m) after $t_2 = 30$ seconds, and (k) and (o) after $t_3 = 50$ seconds, respectively. Scale bars represent 200 μm.

seen in Fig. 5(b), which depicts the measured elasticity over the first minute, representing QME acquisition times used previously [34,37].

To directly illustrate the temporal effect of friction, Figs. 5(c) - 5(o) show the measured strain in the layer and sample for a 1 mm (lateral) × 0.35 mm (axial) region after 10, 30, and 50 seconds for Lubricant 1 (Figs. 5(c) - 5(h)) and Lubricant 3 (Figs. 5(i) - 5(o)), respectively. In Figs. 5(c) - 5(e), for Lubricant 1, we observe a significant temporal decrease from the initial layer strain, with a mean and standard deviation of −2.42 mε ± 0.14 mε, to −2.28 mε ± 0.15 mε after 10 seconds. Further, after 30 seconds we observe a mean strain and standard deviation of −1.92 mε ± 0.15 mε, and after 50 seconds, a mean and standard deviation of −1.66 mε ± 0.14 mε. Comparatively, in Figs. 5(i) - 5(k), for Lubricant 3, we see smaller relative changes from the initial layer strain of −3.12 mε ± 0.16 mε, to −3.11 mε ± 0.16 mε after 10 seconds, and a strain of −3.06 mε ± 0.17 mε and −2.98 mε ± 0.19 mε, after 30 seconds and 50 seconds, respectively. Given that a constant micro-scale strain is applied, the reduction in layer strain as a result of friction leads to an increase in the sample strain. For instance, as seen in Figs. 5(f) - 5(h) for Lubricant 1, the strain in the sample increases from −1.49 mε ± 0.26 mε after 10 seconds, to −1.56 mε ± 0.22 mε after 50 seconds. Similarly, for Lubricant 3 in Figs. 5(l) - 5(o), the sample strain increases from −1.29 mε ± 0.33 mε after 10 seconds, to −1.37 mε ± 0.32 mε after 50 seconds. In the estimation of elasticity in Eqn. 1, a reduction in the layer strain, and correspondingly, the estimated stress, as well as an increase in sample strain, results in an underestimation of the sample elasticity. Therefore, for lubricants of higher viscosity, the increased temporal stability of the layer and sample strain leads to improved temporal stability of the estimated elasticity.

In addition to the temporal stability of the estimated elasticity using lubricants with different viscosities, the accuracy of QME is also affected by the viscosity of the lubricant. The least viscous lubricant (Lubricant 1) was expelled almost immediately during the application of a pre-strain, prior to acquisition, and demonstrated the highest initial error of 29%. Lubricants of higher viscosity (Lubricant 2 and Lubricant 3) showed improved accuracy, with initial errors of 13% and 2% of the expected value, respectively, while the lubricants of highest viscosity (Lubricant 4 and Lubricant 5) demonstrated increasing errors of 13% and 23%, respectively. The increased error for lubricants of higher viscosity, despite the ability to maintain a film of lubricant, is due to the increased transfer of shear stress across the lubricant boundary for higher viscosities.

The results in this section suggest that the choice of lubricant, and most notably the lubricant viscosity, should be optimized for both elasticity accuracy and temporal stability. This is since lubricants of lower viscosity demonstrate rapid exudation, and, therefore, increased friction and degradation of the accuracy of the estimated elasticity. Conversely, lubricants of high viscosity, despite providing improved temporal stability, introduce increased shear stress, and, therefore, friction at the contact boundaries, reducing the accuracy of the estimated elasticity. In general, the optimal choice of lubricant will depend on the specific layer and sample properties, however, for the samples used in this study, Lubricant 3 offers the best trade-off between elasticity accuracy and temporal stability. For this reason, Lubricant 3 was used for the results presented in Sections 4.4 and 4.5.

4.4. Validation of QME on silicone phantoms

In this section, to validate that QME provides accurate elasticity for a wide range of sample elasticity, we performed scans on six silicone phantoms with Young's moduli ranging from 3 kPa (representative of soft tissues such as adipose tissue), to 15 - 40 kPa (characteristic of muscle tissue), to >130 kPa, (representative of certain types of tumors) [1,5,7,45]. For each of the six phantoms, five QME scans were acquired. For all scans, a pre-strain was applied until uniform contact was made between the imaging window, layer and sample. Additionally, to avoid temporal effects, lubricant was re-applied between each consecutive scan. For the optimization
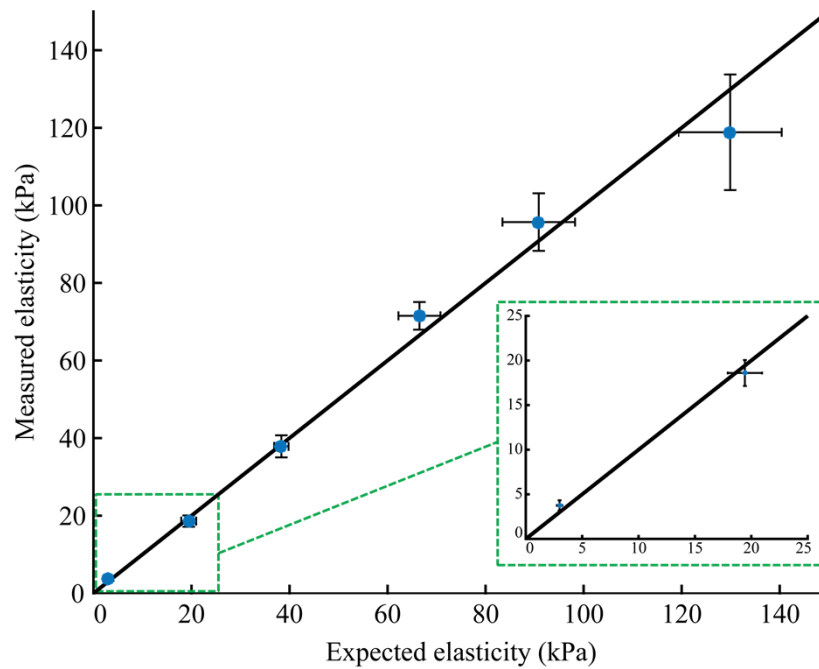
Fig. 6. Validation of QME (measured) on homogeneous silicone phantoms against uniaxial compression testing (expected). The solid black line represents perfect correspondence between the expected and measured elasticity. Inset, magnified plot of the first two measurements.

of QME accuracy, based on the analysis of lubricant viscosity in Section 4.3, Lubricant 3 was applied to all contact surfaces and the acquisition time was <10 seconds. The mean elasticity was estimated from a 1 mm (lateral) × 0.5 mm (axial) region of interest, 100 μm below the sample surface. Figure 6 shows the mean and standard deviation of the five elasticity measurements for each phantom, against the expected elasticity from uniaxial compressing testing. Similarly, the standard deviation of elasticity from uniaxial compression testing is shown by the horizontal error bars in Fig. 6. Additionally, the solid black line represents ideal measurements, corresponding to perfect correlation between the expected and measured elasticity.

Linear fitting of the experimental data yields a coefficient of determination (r^2) of 0.99 and a correlation of 0.98 to the expected values (where a correlation of one indicates perfect correspondence between the measured and expected elasticity), demonstrating high accuracy of QME. The average error between the measured and expected elasticity across the six phantoms is 6.9%. These results validate an optimized QME imaging protocol, namely, using a lubricant of appropriate viscosity (*e.g.*, 100 mm^2s^{-1}) and with sufficiently short acquisition times (*e.g.*, 10 seconds) to allow for accurate elasticity measurements over a wide range of sample elasticity. However, it can also be seen that the precision of the estimated elasticity is degraded with increasing sample elasticity. This can be attributed to increased phase decorrelation noise due to decorrelation of the OCT speckle pattern at higher layer strains, occurring for samples of increasing elasticity. For instance, the resulting strain in the layer for the stiffest sample (~130 kPa) is over 40 times larger compared to that of the softest sample (~3 kPa), consequently degrading elasticity sensitivity, and subsequent precision [33].

4.5. Analysis of friction in a heterogeneous phantom

Thus far, the effects of friction and the development and validation of an optimized QME imaging protocol has been demonstrated on homogeneous phantoms. In this section, we perform QME on a mechanically heterogeneous phantom, demonstrating the impact of friction on the accuracy of the measured elasticity for different lubrication conditions. Resembling Section 4.1, four QME scans were performed, varying the application of lubricant to the contact surfaces. QME was initially performed without lubrication, followed by separate scans with lubrication applied exclusively at the layer-sample interface, the window-layer interface, and both interfaces, respectively. In each case, a pre-strain was applied until uniform contact was made between the imaging window, layer and sample. The QME accuracy was optimized through the application of Lubricant 3 to all contact interfaces, and the acquisition time was <10 seconds in each case. The mean and standard deviation of elasticity was estimated for both the bulk and inclusion from a 500 μm (lateral) × 250 μm (axial) region of interest located at a depth starting 50 μm below the surface of the inclusion. Figure 7 demonstrates the impact of lubrication on heterogeneous samples, where Figs. 7(a) - 7(h) show the OCT and corresponding elastograms for the different lubrication conditions, and Fig. 7(i) shows the mean and standard deviation of elasticity taken from the regions of interest in the bulk and inclusion. To minimize the contribution of noise in the comparison of elastograms, particularly due to increased OCT attenuation in the highly scattering inclusion, Figs. 7(a) - 7(h) correspond to regions in depth with OCT SNR >5 dB (~0.9 mm into the sample).

Similar to Section 4.1, in the case of no lubrication (Figs. 7(a) and 7(b)) and lubrication at the layer-sample interface (Figs. 7(c) and 7(d)), friction between the imaging window and layer results in reduced layer strain, and, thus, an underestimation of the applied stress. Consequently, in both cases, the elasticity measured in the bulk and inclusion is underestimated as being over 8 times lower than the expected elasticity of 38.3 kPa and 66.5 kPa, respectively. For example, in the case of no lubrication (Figs. 7(a) and 7(b)), the mean elasticity and elasticity sensitivity are 4.5 kPa and 0.2 kPa in the bulk, and 8.2 kPa and 0.9 kPa in the inclusion. Lubrication between the imaging window and layer (Figs. 7(e) and 7(f)) allows for increased layer strain, reducing the apparent error in elasticity for the bulk and inclusion to an underestimation by a factor of 2.3. However, as for the homogeneous sample, friction, and, thus, mechanical coupling between the layer and sample leads to the measured sample elasticity in both the bulk and inclusion being heavily influenced by the elasticity of the layer. Finally, for lubrication of all contact surfaces (Figs. 7(g) and 7(h)), the mean elasticity and elasticity sensitivity in the bulk are 39.6 kPa and 6.0 kPa, and 66.1 kPa and 20.0 kPa for the inclusion, a substantial improvement in the elasticity accuracy, corresponding to an overestimation by a factor of 1.03 in the bulk, and underestimation by a factor of 1.01 in the inclusion, errors of 3% and 1%, respectively. The overestimation of elasticity in the bulk, and underestimation of elasticity in the inclusion is likely a result of mechanical coupling, whereby the deformation of the soft bulk is restricted by the stiff inclusion, increasing the apparent elasticity, and vice versa.

In comparison to the other lubrication conditions, lubrication of all contact surfaces leads to a significant improvement in the elasticity accuracy in both the bulk and inclusion, demonstrating the ability of an optimized QME protocol to accurately measure heterogeneous mechanical features. However, analogous to Section 4.1, increased phase decorrelation, a result of lubrication, degrades the elasticity sensitivity in both the bulk and inclusion.
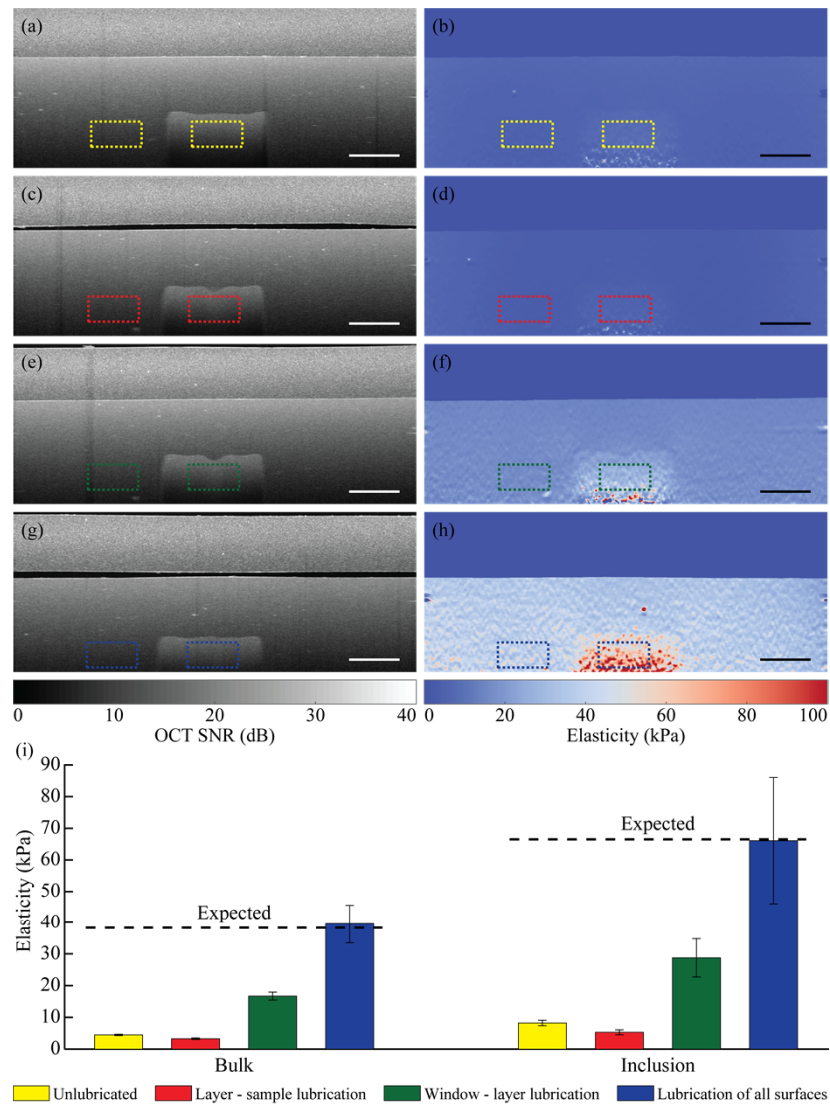
Fig. 7. The impact of lubrication on heterogeneous samples in QME. (a) - (h) depict the OCT and corresponding elastograms for different lubrication conditions, namely: (a) and (b) unlubricated contact surfaces; (c) and (d) lubricant at the layer-sample interface; (e) and (f) lubricant at the window-layer interface; (g) and (h) lubricant at both interfaces. (i) Plot of the mean and standard deviation of elasticity in the bulk and inclusion for different lubrication conditions, illustrated using color-coded bars. Note that the colored, dashed rectangles in each image in (a) - (h) represent the chosen regions of interest for each lubrication condition. Scale bars represent 500 μm.

5. Discussion

In this paper, we presented an analysis of friction in QME. By implementing a series of tests on silicone phantoms, we demonstrated that friction, and the resulting accuracy of QME, is significantly influenced by several experimental factors, including the application of lubricant at the contact surfaces, the viscosity of the lubricant, the time after the application of pre-strain,

and the mechanical contrast between the compliant layer and the sample. Furthermore, we demonstrated the ability to accurately estimate the elasticity of a nonlinear elastic sample over a range of strain, and developed an optimized imaging protocol to minimize the effects of friction. This allowed us to obtain accurate measurements of elasticity, to within 10% error, for homogeneous phantoms with a wide range of mechanical properties, as well as for a mechanically heterogeneous phantom.

In Section 4.1, we demonstrated that lubrication of all contact surfaces was required to reduce friction, resulting in independent layer and sample deformation. Appropriate lubrication allowed for accurate estimation of elasticity, however, despite the improvement in the accuracy of elasticity, the elasticity sensitivity is degraded due to temporal exudation of lubricant, as well as increased phase decorrelation noise in the layer and sample due to lubrication. In particular, the increase in layer strain for the fully lubricated scan in Fig. 3(d), increases translation-induced phase decorrelation in the layer and sample, reducing the elasticity sensitivity. To mitigate the effects of phase decorrelation, previous QME publications have utilized layers and samples with matched mechanical properties [29,33,45]. By matching the elasticity of the layer and sample, the strain SNR in the layer and sample is optimized, improving elasticity sensitivity. As such, in a given application, the elasticity of the layer should be selected to best match the expected sample elasticity. Furthermore, by matching the mechanical properties of the layer and sample, the relative lateral deformation at the layer-sample boundary is reduced, minimizing shear stresses due to friction, and improving elasticity accuracy.

One possible method to mitigate the effects of friction and achieve accurate elasticity results in QME is through characterization of the layer under frictional conditions, compensating for the restriction of the layer deformation in the estimation of elasticity. However, in practice, such frictional characterization of the layer is non-trivial, depending on a multitude of different factors, including the relative difference in mechanical properties between the layer and sample, the geometry of the layer and sample, the lubricant viscosity, the magnitude of applied pre-strain, and the time after pre-strain was applied. As such, compensation for friction would be impractical, requiring each combination of the above factors to be individually characterized. However, for flat samples where uniform layer and sample stresses are expected, it may be possible to perform *in-situ* layer characterization, where the layer is characterized simultaneously with acquisition using a load cell. Alternatively, compensation for friction using a modified mechanical model, or numerical techniques, as proposed by Wijesinghe *et al.* [58] could be used to improve the accuracy of the estimated elasticity. On the other hand, several other quantitative compression OCE techniques have been demonstrated without the use of a compliant layer, potentially reducing friction by minimizing the number of contact boundaries. However, these techniques have been limited to measuring a single value of applied stress, and, therefore, cannot measure spatially resolved stress at the sample surface, or can only provide a one dimensional measurement of elasticity [61,62].

In Section 4.2, QME scans were performed over a range of sample pre-strains. It was demonstrated that without repeated lubrication, the estimated elasticity shows significant temporal dependence due to the exudation of lubricant between acquisitions. However, the use of repeated lubrication between pre-strains allowed for accurate estimation of the nonlinear elastic sample response. As such, repeated lubrication, or otherwise, cumulative loading using rapid acquisition, is recommended for techniques such as nonlinear OCE, where the aim is to use the nonlinear elastic mechanical properties of tissue at increasing pre-strain to provide additional contrast [39].

In Section 4.3, it was demonstrated that the viscosity of the lubricant is an important consideration in the optimization of the estimated elasticity in QME. Broadly, the results show that the temporal stability of the estimated elasticity is proportional to lubricant viscosity *i.e.*, lubricants of higher viscosity show better temporal stability, however, simultaneously allow for increased transfer of shear stresses, impacting the accuracy of estimated elasticity. Hence, the

lubricant viscosity should be carefully considered to optimize the trade-off between the accuracy and stability of the measured elasticity. It should also be noted that the rate of lubricant exudation, and, therefore, the level of friction, in addition to lubricant viscosity, is likely dependent on the applied pre-strain. For instance, at increasingly higher pre-strain, it is expected that the lubricant will be exuded from the contact boundaries more rapidly, reducing the temporal stability of QME. Equally, the use of lower pre-strain is likely to improve the temporal stability, and, thus, QME accuracy over comparable acquisition times. Nonetheless, regardless of the lubricant viscosity, to optimize elasticity accuracy and avoid temporal variations in the estimated elasticity, scans should be acquired as rapidly as possible. Previous studies have also utilized a variety of different lubricants such as glycerol [35] and saline [37] for lubrication of the contact surfaces. As such, in a future study, it may be useful to examine the effects of friction for lubricants with different characteristics, for instance, properties such as hydrophobicity and hydrophilicity. It should be noted that in addition to lubricant viscosity, temporal variations in the estimated elasticity can be affected by the viscoelastic response of silicone and tissue. To minimize the contribution of viscoelasticity in the estimation of elasticity in Section 4.3, minimal pre-strain was applied to the layer and sample. In addition, prior characterization of both the magnitude and temporal duration of the viscoelastic strain response for silicones such as those used in this study were shown to be an order of magnitude lower than those shown in Section 4.3 [63]. As a result, the contribution of viscoelasticity to temporal variations in the estimated elasticity was deemed to be negligible in comparison to the effect of lubricant viscosity.

This study has limited the investigation of friction to flat samples with well controlled geometry, such as those commonly investigated in mechanobiology [36,42]. However, many tissue samples have non-regular geometries, *i.e.*, surface roughness, which may introduce variable friction that depends on the surface topography of the sample. In addition, tissue is mainly comprised of water, and, as such, may elicit different frictional behavior, requiring different types of lubricants to those presented here for silicone phantoms. However challenging, future studies should investigate the impact of friction on tissue, as well as samples with irregular surface geometry. In addition, future research could be conducted to explore other friction minimization techniques, such as the implementation of low coefficient of friction coatings such as polytetrafluoroethylene.

6. Conclusion

This work presents a framework to analyze the effects of friction on the accuracy of QME, enabling the optimization of sample-specific imaging protocols for more accurate and robust estimations of elasticity. We analyzed the effect of different lubrication conditions, demonstrating that friction introduces systematic errors in the estimation of sample elasticity, requiring lubrication of all contact surfaces to achieve an accurate estimation of elasticity. We demonstrated the ability to accurately assess the nonlinear elastic response of a phantom over a range of pre-strains, and through an analysis of lubricant viscosities, developed and validated an optimized QME imaging protocol capable of obtaining accurate estimates of elasticity for samples with Young's moduli ranging over an order of magnitude. We believe that the presented framework enables a better understanding of the effects of friction in compression OCE and provides a foundation to study the impact of friction in contact-based elastography techniques more generally.

References

1. C. F. Guimarães, L. Gasperini, A. P. Marques, and R. L. Reis, "The stiffness of living tissues and its implications for tissue engineering," Nat. Rev. Mater. **5**(5), 351–370 (2020).
2. B. F. Kennedy, P. Wijesinghe, and D. D. Sampson, "The emergence of optical elastography in biomedicine," Nat. Photonics **11**(4), 215–221 (2017).
3. M. C. Lampi and C. A. Reinhart-King, "Targeting extracellular matrix stiffness to attenuate disease: From molecular mechanisms to clinical trials," Sci. Transl. Med. **10**(422), eaao0475 (2018).
4. N. M. E. Ayad, S. Kaushik, and V. M. Weaver, "Tissue mechanics, an important regulator of development and disease," Philos. Trans. R. Soc., B **374**(1779), 20180215 (2019).
5. T. A. Krouskop, T. M. Wheeler, F. Kallel, B. S. Garra, and T. Hall, "Elastic moduli of breast and prostate tissues under compression," Ultrason. Imaging **20**(4), 260–274 (1998).
6. A. E. Bohte, J. L. Nelissen, J. H. Runge, O. Holub, S. A. Lambert, L. de Graaf, S. Kolkman, S. van der Meij, J. Stoker, G. J. Strijkers, A. J. Nederveen, and R. Sinkus, "Breast magnetic resonance elastography: a review of clinical work and future perspectives," NMR Biomed. **31**(10), e3932 (2018).
7. A. Samani, J. Zubovits, and D. Plewes, "Elastic moduli of normal and pathological human breast tissues: an inversion-technique-based investigation of 169 samples," Phys. Med. Biol. **52**(6), 1565–1576 (2007).
8. M. Tölle, A. Reshetnik, M. Schuchardt, M. Höhne, and M. van der Giet, "Arteriosclerosis and vascular calcification: causes, clinical assessment and therapy," Eur. J. Clin. Invest. **45**(9), 976–985 (2015).
9. H. H. Dao, R. Essalihi, C. Bouvet, and P. Moreau, "Evolution and modulation of age-related medial elastocalcinosis: Impact on large artery stiffness and isolated systolic hypertension," Cardiovasc. Res. **66**(2), 307–317 (2005).
10. M. Kanbay, B. Afsar, P. Gusbeth-Tatomir, and A. Covic, "Arterial stiffness in dialysis patients: where are we now?" Int. Urol. Nephrol. **42**(3), 741–752 (2010).
11. M. Li, D. Dang, L. Liu, N. Xi, and Y. Wang, "Atomic force microscopy in characterizing cell mechanics for biomedical applications: a review," IEEE Trans. NanoBiosci. **16**(6), 523–540 (2017).
12. M. Krieg, G. Fläschner, D. Alsteens, B. M. Gaub, W. H. Roos, G. J. L. Wuite, H. E. Gaub, C. Gerber, Y. F. Dufrêne, and D. J. Müller, "Atomic force microscopy-based mechanobiology," Nat. Rev. Phys. **1**(1), 41–57 (2018).
13. J. Zemła, J. Danilkiewicz, B. Orzechowska, J. Pabijan, S. Seweryn, and M. Lekka, "Atomic force microscopy as a tool for assessing the cellular elasticity and adhesiveness to identify cancer cells and tissues," Semin. Cell Dev. Biol. **73**, 115–124 (2018).
14. R. M. S. Sigrist, J. Liau, A. E. Kaffas, M. C. Chammas, and J. K. Willmann, "Ultrasound elastography: review of techniques and clinical applications," Theranostics **7**(5), 1303–1329 (2017).
15. Y. K. Mariappan, K. J. Glaser, and R. L. Ehman, "Magnetic resonance elastography: A review," Clin. Anat. **23**(5), 497–511 (2010).
16. K. V. Larin and D. D. Sampson, "Optical coherence elastography – OCT at work in tissue biomechanics," Biomed. Opt. Express **8**(2), 1172–1202 (2017).
17. C. Sun, B. A. Standish, and V. X. D. Yang, "Optical coherence elastography: current status and future applications," J. Biomed. Opt. **16**(4), 043001 (2011).
18. B. F. Kennedy, K. M. Kennedy, and D. D. Sampson, "A review of optical coherence elastography: fundamentals, techniques and prospects," IEEE J. Sel. Top. Quantum Electron. **20**(2), 272–288 (2014).
19. A. Jiménez-villar, E. Mączyńska, A. Cichański, M. Wojtkowski, B. J. Kałużny, and I. Grulkowski, "High-speed OCT-based ocular biometer combined with an air-puff system for determination of induced retraction-free eye dynamics," Biomed. Opt. Express **10**(7), 3663–3680 (2019).
20. S. Wang and K. V. Larin, "Noncontact depth-resolved micro-scale optical coherence elastography of the cornea," Biomed. Opt. Express **5**(11), 3807–3821 (2014).
21. H.-C. Liu, M. Abbasi, Y. H. Ding, T. Roy, M. Capriotti, Y. Liu, S. Fitzgerald, K. M. Doyle, M. Guddati, M. W. Urban, and W. Brinjikji, "Characterizing blood clots using acoustic radiation force optical coherence elastography and ultrasound shear wave elastography," Phys. Med. Biol. **66**(3), 035013 (2021).
22. X. Xu, J. Zhu, and Z. Chen, "Dynamic and quantitative assessment of blood coagulation using optical coherence elastography," Sci. Rep. **6**(1), 24294 (2016).
23. B. F. Kennedy, R. A. McLaughlin, K. M. Kennedy, L. Chin, P. Wijesinghe, A. Curatolo, A. Tien, M. Ronald, B. Latham, C. M. Saunders, and D. D. Sampson, "Investigation of optical coherence microelastography as a method to visualize cancers in human breast tissue," Cancer Res. **75**(16), 3236–3245 (2015).
24. E. V. Gubarkova, E. B. Kiseleva, M. A. Sirotkina, D. A. Vorontsov, K. A. Achkasova, S. S. Kuznetsov, K. S. Yashin, A. L. Matveyev, A. A. Sovetsky, L. A. Matveev, A. A. Plekhanov, A. Y. Vorontsov, V. Y. Zaitsev, and N. D. Gladkova, "Diagnostic accuracy of cross-polarization OCT and OCT-elastography for differentiation of breast cancer subtypes: comparative study," Diagnostics **10**(12), 994 (2020).
25. W. M. Allen, L. Chin, P. Wijesinghe, R. W. Kirk, B. Latham, D. D. Sampson, C. M. Saunders, and B. F. Kennedy, "Wide-field optical coherence micro-elastography for intraoperative assessment of human breast cancer margins," Biomed. Opt. Express **7**(10), 4139–4153 (2016).
26. W. M. Allen, K. M. Kennedy, Q. Fang, L. Chin, A. Curatolo, L. Watts, R. Zilkens, S. L. Chin, B. F. Dessauvagie, B. Latham, C. M. Saunders, and B. F. Kennedy, "Wide-field quantitative micro-elastography of human breast tissue," Biomed. Opt. Express **9**(3), 1082–1096 (2018).

27. V. Y. Zaitsev, A. L. Matveyev, L. A. Matveev, A. A. Sovetsky, M. S. Hepburn, A. Mowla, and B. F. Kennedy, "Strain and elasticity imaging in compression optical coherence elastography: The two-decade perspective and recent advances," J. Biophotonics **14**, e202000257 (2021).

28. B. F. Kennedy, R. A. McLaughlin, K. M. Kennedy, L. Chin, A. Curatolo, A. Tien, B. Latham, C. M. Saunders, and D. D. Sampson, "Optical coherence micro-elastography: mechanical-contrast imaging of tissue microstructure," Biomed. Opt. Express **5**(7), 2113–2124 (2014).

29. K. M. Kennedy, L. Chin, R. A. McLaughlin, B. Latham, C. M. Saunders, D. D. Sampson, and B. F. Kennedy, "Quantitative micro-elastography: imaging of tissue elasticity using compression optical coherence elastography," Sci. Rep. **5**(1), 15538 (2015).

30. A. A. Plekhanov, M. A. Sirotkina, A. A. Sovetsky, E. V. Gubarkova, S. S. Kuznetsov, A. L. Matveyev, L. A. Matveev, E. V. Zagaynova, N. D. Gladkova, and V. Y. Zaitsev, "Histological validation of in vivo assessment of cancer tissue inhomogeneity and automated morphological segmentation enabled by optical coherence elastography," Sci. Rep. **10**(1), 11781 (2020).

31. V. Y. Zaitsev, A. L. Matveyev, L. A. Matveev, G. V. Gelikonov, A. A. Sovetsky, and A. Vitkin, "Optimized phase gradient measurements and phase-amplitude interplay in optical coherence elastography," J. Biomed. Opt. **21**(11), 116005 (2016).

32. A. A. Sovetsky, A. L. Matveyev, L. A. Matveev, D. V. Shabanov, and V. Y. Zaitsev, "Manually-operated compressional optical coherence elastography with effective aperiodic averaging: demonstrations for corneal and cartilaginous tissues," Laser Phys. Lett. **15**(8), 085602 (2018).

33. J. Li, M. S. Hepburn, L. Chin, A. Mowla, and B. F. Kennedy, "Analysis of sensitivity in quantitative micro-elastography," Biomed. Opt. Express **12**(3), 1725–1745 (2021).

34. Q. Fang, B. Krajancich, L. Chin, R. Zilkens, A. Curatolo, L. Frewer, J. D. Anstie, P. Wijesinghe, C. Hall, B. F. Dessauvagie, B. Latham, C. M. Saunders, and B. F. Kennedy, "Handheld probe for quantitative micro-elastography," Biomed. Opt. Express **10**(8), 4034–4049 (2019).

35. V. Y. Zaitsev, A. L. Matveyev, L. A. Matveev, E. V. Gubarkova, A. A. Sovetsky, M. A. Sirotkina, G. V. Gelikonov, E. V. Zagaynova, N. D. Gladkova, and A. Vitkin, "Practical obstacles and their mitigation strategies in compressional optical coherence elastography of biological tissues," J. Innovative Opt. Health Sci. **10**(06), 1742006 (2017).

36. A. Mowla, J. Li, M. S. Hepburn, S. Maher, L. Chin, G. C. Yeoh, Y. S. Choi, and B. F. Kennedy, "Subcellular mechano-microscopy: high resolution three-dimensional elasticity mapping using optical coherence microscopy," Opt. Lett. **47**(13), 3303–3306 (2022).

37. P. Gong, S. L. Chin, and W. M. Allen, *et al.*, "Quantitative micro-elastography enables in vivo detection of residual cancer in the surgical cavity during breast-conserving surgery," Cancer Res. **82**(21), 4093–4104 (2022).

38. K. M. Kennedy, R. Zilkens, and W. M. Allen, *et al.*, "Diagnostic accuracy of quantitative micro-elastography for margin assessment in breast-conserving surgery," Cancer Res. **80**(8), 1773–1783 (2020).

39. E. V. Gubarkova, A. A. Sovetsky, L. A. Matveev, A. L. Matveyev, D. A. Vorontsov, A. A. Plekhanov, S. S. Kuznetsov, S. V. Gamayunov, A. Y. Vorontsov, M. A. Sirotkina, N. D. Gladkova, and V. Y. Zaitsev, "Nonlinear elasticity assessment with optical coherence elastography for high-selectivity differentiation of breast cancer tissues," Materials **15**(9), 3308 (2022).

40. E. V. Gubarkova, A. A. Sovetsky, D. A. Vorontsov, P. A. Buday, M. A. Sirotkina, A. A. Plekhanov, S. S. Kuznetsov, A. L. Matveyev, L. A. Matveev, S. V. Gamayunov, A. Y. Vorontsov, V. Y. Zaitsev, and N. D. Gladkova, "Compression optical coherence elastography versus strain ultrasound elastography for breast cancer detection and differentiation: pilot study," Biomed. Opt. Express **13**(5), 2859–2881 (2022).

41. E. V. Gubarkova, A. A. Sovetsky, V. Y. Zaitsev, A. L. Matveyev, D. A. Vorontsov, M. A. Sirotkina, L. A. Matveev, A. A. Plekhanov, N. P. Pavlova, S. S. Kuznetsov, A. Y. Vorontsov, E. V. Zagaynova, and N. D. Gladkova, "OCT-elastography-based optical biopsy for breast cancer delineation and express assessment of morphological/molecular subtypes," Biomed. Opt. Express **10**(5), 2244–2263 (2019).

42. M. S. Hepburn, P. Wijesinghe, L. G. Major, J. Li, A. Mowla, C. Astell, H. W. Park, Y. Hwang, Y. S. Choi, and B. F. Kennedy, "Three-dimensional imaging of cell and extracellular matrix elasticity using quantitative micro-elastography," Biomed. Opt. Express **11**(2), 867–884 (2020).

43. P. Wijesinghe, L. Chin, and B. F. Kennedy, "Strain tensor imaging in compression optical coherence elastography," IEEE J. Sel. Top. Quantum Electron. **25**(1), 1–12 (2019).

44. M. S. Hepburn, P. Wijesinghe, L. Chin, and B. F. Kennedy, "Analysis of spatial resolution in phase-sensitive compression optical coherence elastography," Biomed. Opt. Express **10**(3), 1496–1513 (2019).

45. R. W. Sanderson, A. Curatolo, P. Wijesinghe, L. Chin, and B. F. Kennedy, "Finger-mounted quantitative micro-elastography," Biomed. Opt. Express **10**(4), 1760–1773 (2019).

46. S. Achanta, T. Liskiewicz, D. Drees, and J.-P. Celis, "Friction mechanisms at the micro-scale," Tribol. Int. **42**(11-12), 1792–1799 (2009).

47. E. Broitman, "The nature of the frictional force at the macro-, micro-, and nano-scales," Friction **2**(1), 40–46 (2014).

48. K. M. Kennedy, C. Ford, B. F. Kennedy, M. B. Bush, and D. D. Sampson, "Analysis of mechanical contrast in optical coherence elastography," J. Biomed. Opt. **18**(12), 121508 (2013).

49. L. Chin, A. Curatolo, B. F. Kennedy, B. J. Doyle, P. R. T. Munro, R. A. McLaughlin, and D. D. Sampson, "Analysis of image formation in optical coherence elastography using a multiphysics approach," Biomed. Opt. Express **5**(9), 2913–2930 (2014).

50. J. Yang, L. Yu, L. Wang, W. Wang, and J. Cui, "The estimation method of friction in unconfined compression tests of liver tissue," Proc. Inst. Mech. Eng., Part H **232**(6), 573–587 (2018).

51. X. G. Fan, Y. D. Dong, H. Yang, P. F. Gao, and M. Zhan, "Friction assessment in uniaxial compression test: A new evaluation method based on local bulge profile," J. Mater. Process. Technol. **243**, 282–290 (2017).

52. S. Solhjoo and S. Khoddam, "Evaluation of barreling and friction in uniaxial compression test: a kinematic analysis," Int. J. Mech. Sci. **156**, 486–493 (2019).

53. K. J. Parker, L. S. Taylor, S. Gracewski, and D. J. Rubens, "A unified view of imaging the elastic properties of tissue," J. Acoust. Soc. Am. **117**(5), 2705–2712 (2005).

54. B. F. Kennedy, S. H. Koh, R. A. McLaughlin, K. M. Kennedy, P. R. T. Munro, and D. D. Sampson, "Strain estimation in phase-sensitive optical coherence elastography," Biomed. Opt. Express **3**(8), 1865–1879 (2012).

55. G. Lamouche, B. F. Kennedy, K. M. Kennedy, C.-E. Bisaillon, A. Curatolo, G. Campbell, V. Pazos, and D. D. Sampson, "Review of tissue simulating phantoms with controllable optical, mechanical and structural properties for use in optical coherence tomography," Biomed. Opt. Express **3**(6), 1381–1398 (2012).

56. K. M. Kennedy, S. Es'haghian, L. Chin, R. A. McLaughlin, D. D. Sampson, and B. F. Kennedy, "Optical palpation: optical coherence tomography-based tactile imaging using a compliant sensor," Opt. Lett. **39**(10), 3014–3017 (2014).

57. L. Dong, P. Wijesinghe, J. T. Dantuono, D. D. Sampson, P. R. T. Munro, B. F. Kennedy, and A. A. Oberai, "Quantitative compression optical coherence elastography as an inverse elasticity problem," IEEE J. Sel. Top. Quantum Electron. **22**(3), 277–287 (2016).

58. P. Wijesinghe, D. D. Sampson, and B. F. Kennedy, "Computational optical palpation: a finite-element approach to micro-scale tactile imaging using a compliant sensor," J. R. Soc. Interface **14**(128), 20160878 (2017).

59. M. Roegiers and B. Zhmud, "Property blending relationships for binary mixtures of mineral oil and elektrionised vegetable oil: viscosity, solvent power, and seal compatibility index," Lubr. Sci. **23**(6), 263–278 (2011).

60. Y. Qiu, F. R. Zaki, N. Chandra, S. A. Chester, and X. Liu, "Nonlinear characterization of elasticity using quantitative optical coherence elastography," Biomed. Opt. Express **7**(11), 4702–4710 (2016).

61. X. Yao, D. Li, H.-C. Park, D. Chen, H. Guan, M. Mahendroo, and X. Li, "Ultra-sensitive optical coherence elastography using a high-dynamic-range force loading scheme for cervical rigidity assessment," Biomed. Opt. Express **11**(2), 688–698 (2020).

62. Y. Qiu, Y. Wang, Y. Xu, N. Chandra, J. Haorah, B. Hubbi, B. J. Pfister, and X. Liu, "Quantitative optical coherence elastography based on fiber-optic probe for in situ measurement of tissue mechanical properties," Biomed. Opt. Express **7**(2), 688–700 (2016).

63. P. Wijesinghe, R. A. McLaughlin, D. D. Sampson, and B. F. Kennedy, "Parametric imaging of viscoelasticity using optical coherence elastography," Phys. Med. Biol. **60**(6), 2293–2307 (2015).